THE JOURNAL OF PHYSICAL CHEMISTRY C

Article

Cite This: J. Phys. Chem. C 2018, 122, 25051−25058

pubs.acs.org/JPCC

Non-Condon Effects in the Resonance Hyper-Raman Scattering of Chalcogen-Substituted Rhodamine Derivatives

Jacob E. Olson,[†] Alicia Tripp,[‡] Michelle K. Linder,[§] Zhongwei Hu,[‡] Michael R. Detty,*[,§] Lasse Jensen,*[,‡] and Jon P. Camden*[,†]

[†]Department of Chemistry and Biochemistry, University of Notre Dame, Notre Dame, Indiana 46556-5670, United States

[‡]Department of Chemistry, The Pennsylvania State University, 104 Chemistry Building, University Park, Pennsylvania 16802-4615, United States

[§]Department of Chemistry, University at Buffalo, The State University of New York, Buffalo, New York 14260-3000, United States

Supporting Information

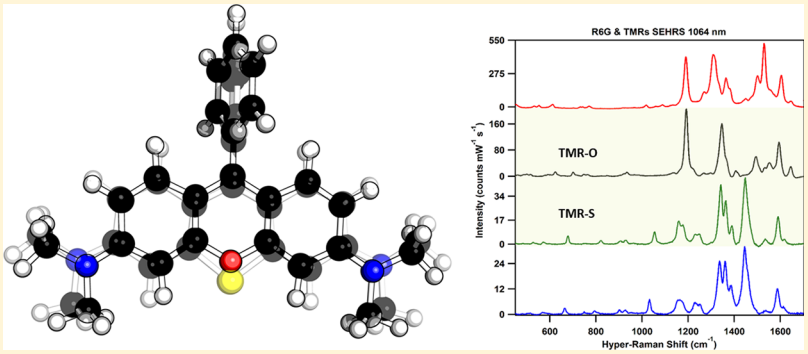

ABSTRACT: Molecules with a strong two-photon response have gained significant interest because of their applications in two-photon imaging, all-optical switching, and energy up-conversion. The surface-enhanced hyper-Raman scattering (SEHRS) of tetramethyl chalcogenorosamines are taken on- and off-resonance and compared to time-dependent density functional theory calculations. Specifically, changes in the SEHRS spectra are tracked as a function of structural geometry because of perturbations induced by larger chalcogen atom substitutions to the xanthene ring. Here we show that the spectral changes and non-Condon effects can be understood by tracking the vibrational normal modes and the vibrationally induced changes to the highest occupied molecular orbitals. With a system in place to explore the relationship between structural geometry and nonlinear properties, various rhodamine derivatives can be characterized as a means to optimally design a series of two-photon bright compounds.

INTRODUCTION

Molecules with a strong two-photon response have gained significant interest because of their applications in two-photon imaging,[1−5] all-optical switching,[6−8] and energy up-conversion.[9−11] The up-conversion afforded by multiphoton processes provides multiple benefits; for example, the use of near infrared lasers allows imaging to be done at higher sampling depths, the detected radiation is easily discernible from interferences, and photobleaching is reduced.[12] One drawback of multiphoton techniques, however, is the poor photon conversion efficiency associated with nonlinear processes. The availability of a class of structurally variant, two-photon bright, molecules, therefore would greatly increase the range of two-photon-based applications. In this work, we undertake a comprehensive experimental and theoretical study of the nonlinear response of chalcogen-substituted rhodamine derivatives, thereby providing a step toward the rational molecular design of two-photon chromophores.

Hyper-Raman (HR) scattering has emerged as a powerful tool for probing the two-photon molecular response.[13] The origin of HR scattering is understood classically by considering the expansion of the induced dipole moment (μ_i) in terms of the driving electric field (E_i)

$$\mu_i = \alpha_{ij}E_j + \frac{1}{2}\beta_{ijk}E_jE_k + \ldots \quad (1)$$

In this expansion, the polarizability tensor, α, leads to Rayleigh and Raman scattering and the hyperpolarizability tensor, β, leads to hyper-Rayleigh and HR scattering. For vibrational HR scattering, two photons interact with a molecule through a virtual state, resulting in one HR scattered photon which has lost energy because of a vibrational excitation

Received: August 2, 2018
Revised: October 4, 2018
Published: October 4, 2018

DOI: 10.1021/acs.jpcc.8b07507
J. Phys. Chem. C 2018, 122, 25051−25058

$$\omega_{HR} = 2\omega_i - \omega_{vib} \quad (2)$$

The selection rules imposed by β are unique when compared with other vibrational spectroscopies; for example, allowing modes which are IR and Raman inactive to become HR active.[14] Therefore, HR scattering provides unique vibrational information as well as access to states that are one-photon inaccessible. Because HR is an inherently weak process, about 10^6 times weaker than Raman scattering under typical conditions, additional signal enhancement is necessary. Surface-enhanced HR scattering (SEHRS) can greatly enhance the signal, on the order of 10^{13}, via analyte adsorption to a plasmonic substrate.[15,16] With this intense enhancement, SEHRS becomes an applicable method for trace analyte detection, even reaching the single-molecule level.[17,18]

The interplay between electronic and vibrational degrees of freedom can be obtained from SEHRS spectra taken on-resonance with an electronic state.[19] Under resonance conditions, the hyperpolarizability tensor can be expanded using the sum-over-states formalism as:

$$\beta = A + B \quad (3)$$

where A and B are the Franck−Condon and Herzberg−Teller terms, respectively.[20,21] Franck−Condon scattering (A-term) often dominates in noncentrosymmetric molecules, where the one- and two-photon transitions are both allowed.[22] B-term contributions, however, appear when either the one- or two-photon dipole moment transition, $\boldsymbol{\mu}$ or $\mathbf{S}$, is disallowed, requiring the transition to occur through its molecular coordinate derivatives, $\frac{\partial \boldsymbol{\mu}}{\partial Q}$ or $\frac{\partial \mathbf{S}}{\partial Q}$. B-term contributions are often 100 times weaker than their A-term counterparts in resonance HR (RHR), yet they can dominate the spectra when A-term activity is symmetry forbidden, as is the case for centrosymmetric molecules.[20] B-term activity provides rich information about vibrational coupling and interference effects between excited states. Specifically, vibronically coupled modes have the ability to perturb electronic state symmetry, thus providing additional scattering intensity via resonance enhancement. To date, however, B-term activity has yet to be systematically explored for structurally variant two-photon bright molecules.

Rhodamine 6G (R6G), a xanthene-based dye, and various modifications thereof have been widely studied because of their impressive photostability and one- and two-photon response.[23,24] Interestingly, R6G retains centrosymmetric symmetry in its lowest lying electronic state and therefore does not exhibit strong A-term HR scattering, and previous studies have concluded that non-Condon and interference effects dominate its nonlinear scattering response.[25] Specifically, the asymmetric 1535 cm^{-1} vibrational mode perturbs the highest occupied molecular orbital (HOMO) and HOMO − 1 orbitals enough to break the symmetry, causing both $S_1 \leftarrow S_0$ and $S_2 \leftarrow S_0$ transitions to gain intensity through B-term activity.[26] In the case of R6G, the B-term contribution is ∼300× more intense than the A-term, causing R6G to be an unexpectedly efficient HR scatterer.[25] In fact, despite its lack of A-term activity, the RHR scattering cross section of R6G can rival that of strongly A-term-dominated molecules such as *para*-nitroanaline.[21] Systematic variation of the R6G structure and subsequent exploitation of the non-Condon scattering might present a new approach toward optimizing the nonlinear molecular response and the design of brighter SEHRS tags.

In this work, we present a comprehensive experimental and theoretical study of the SEHRS response of chalcogen-substituted rhodamine derivatives. Specifically, the tetramethyl chalcogenorosamines (**TMR-E**), seen in Scheme 1, are variations of tetramethylrosamine (**TMR-O**) where the oxygen in the xanthene ring is substituted with sulfur (**TMR-S**) or selenium (**TMR-Se**). The change in nonlinear response brought about by the chalcogen is tracked to correlate structure with the SEHRS and track the vibrational modes contributing to strong B-term activity. Unraveling the nonlinear scattering mechanism of systematically designed xanthene-based molecules through SEHRS and theoretical calculation is the first step toward the optimal design of efficient two-photon tags relying on non-Condon scattering.

Scheme 1. Synthesis of the Tetramethyl Chalcogenorosamines (TMR-E, E = O, S, Se)

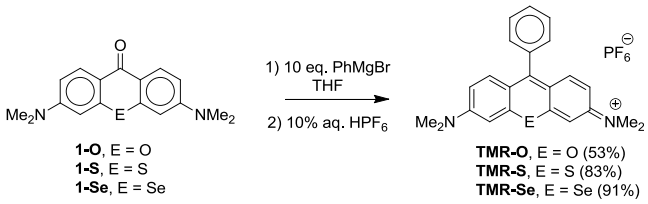

METHODS

Synthesis. The tetramethyl chalcogenorosamines (**TMR-E**, E = O, S, Se) as the hexafluorophosphate salts have been previously reported.[27,28] We prepared these molecules using a slight modification of the reported procedure as shown in Scheme 1. A 10-fold excess of PhMgBr was added to the corresponding 3,6-bis(dimethylamino)-9*H*-chalcogenoxanthen-9-one (**1-O**,[29] **1-S**,[30] **1-Se**[30]) followed by quenching with aqueous 10% HPF_6 to give **TMR-O**, **TMR-S**, and **TMR-Se** in 53, 83, and 91% isolated yields, respectively.

Preparation of TMR-O.[27] Phenylmagnesium bromide (3.54 mL of a 1 M solution, 3.54 mmol) was added dropwise to a stirred suspension of 3,6-bis(dimethylamino)-9*H*-xanthen-9-one[29] (**1-O**, 0.10 g, 0.354 mmol) in tetrahydrofuran (THF) (25 mL) in a flame-dried flask under nitrogen. The resulting solution was heated to 65 °C for 16 h and then cooled to room temperature before being poured into 25 mL of 10% (by weight) aqueous HPF_6. The product was then extracted with dichloromethane (3 × 25 mL), concentrated, and recrystallized from hot acetonitrile to yield **TMR-O**[28] as a green solid (0.065 g, 53%), mp > 260 °C: ^{1}H NMR (500 MHz, CD_2Cl_2): δ 7.72−7.60 (m, 3H), 7.48−7.36 (m, 4H), 6.93 (dd, 2H, J = 2.0, 9.5 Hz), 6.83 (d, 2H, J = 2.0 Hz), 3.30 (s, 12 H); ^{13}C NMR (75.5 MHz, CD_2Cl_2): δ 158.9, 158.3, 157.7, 132.2, 130.8, 129.9, 129.2, 115.6, 114.5, 113.9, 96.9, 41.1; λ_{max} (MeOH) nm: 536 nm (ε = 1.08 × 10^5 M^{-1} cm^{-1}). λ_{max} (CD_2Cl_2): 538 nm (ε = 1.08 × 10^5 M^{-1} cm^{-1}). HRMS (ESI) m/z: 343.18054 (calcd for $C_{23}H_{23}N_2O^+$, 343.18049).

Preparation of TMR-S.[27,28] Phenylmagnesium bromide (3.35 mL of a 1 M solution, 3.35 mmol) was added dropwise to a stirred suspension of 3,6-bis(dimethylamino)-9*H*-thioxanthen-9-one[30] (**1-S**, 0.10 g, 0.335 mmol, 1.0 equiv) in THF (25 mL) in a flame-dried flask under nitrogen. The resulting solution was heated to 65 °C for 16 h, then cooled to room temperature before being poured into 25 mL of 10% (by weight) aqueous HPF_6. The product was extracted with

DOI: 10.1021/acs.jpcc.8b07507
J. Phys. Chem. C 2018, 122, 25051−25058

dichloromethane (3 × 25 mL), concentrated, and recrystallized from acetonitrile/diethyl ether to yield **TMR-S**[27,28] as a green solid (0.140 g, 0.278 mmol, 83%), mp > 260 °C: ^{1}H NMR (500 MHz, CD_2Cl_2): δ 7.70−7.58 (m, 3H), 7.43 (d, 2H, J = 9.5 Hz), 7.38−7.29 (m, 2H), 7.11 (d, 2H, J = 2.5 Hz), 6.92 (dd, 2H, J = 2.5, 9.5 Hz), 3.28 (s, 12H); ^{13}C NMR (75.5 MHz, CD_2Cl_2): δ 153.5, 144.4, 136.5, 135.4, 129.5, 129.2, 128.7, 119.2, 115.1, 114.2, 105.4, 40.5; λ_{max} (MeOH): 557 nm (ε = 9.44 × 10^4 M^{-1} cm^{-1}). λ_{max} (CD_2Cl_2): 557 nm (ε = 7.95 × 10^4 M^{-1} cm^{-1}); HRMS (ESI) m/z: 359.1577 (calcd for $C_{23}H_{23}N_2S^+$, 359.1576).

Preparation of TMR-Se.[27,28] Bromobenzene (0.475 mL, 4.34 mmol) was added to a stirred suspension of magnesium (0.12 g, 4.92 mmol) in THF (3 mL). The mixture was stirred at ambient temperature for 1 h, and the resulting Grignard solution was transferred via cannula to a stirred suspension of 3,6-bis(dimethylamino)-9*H*-selenoxanthen-9-one[30] (**1-Se**, 0.10 g, 0.290 mmol) in THF (7 mL). The resulting solution was heated to 65 °C for 16 h, then cooled to room temperature before being poured into 25 mL of 10% (by weight) aqueous HPF_6. After 12 h, the resulting precipitate was collected via vacuum filtration and washed with water (5 mL) and diethyl ether (15 mL). The acetonitrile soluble material was removed and recrystallized in acetonitrile/diethyl ether to yield **TMR-Se**[27,28] as a green solid (0.146 g, 0.265 mmol, 91%), mp > 260 °C: ^{1}H NMR (500 MHz, CD_2Cl_2): δ 7.66−7.56 (m, 3H), 7.43 (d, 2 H, J = 10.0 Hz), 7.34−7.25 (m, 4H), 6.83 (dd, 2H, J = 2.5, 10.0 Hz), 3.25 (s, 12 H); ^{13}C NMR (75.5 MHz, CD_2Cl_2): δ 161.3, 152.6, 146.1, 138.1, 136.9, 128.9, 128.8, 128.3, 119.6, 114.4, 109.2, 40.4; λ_{max} (MeOH): 568 nm (ε = 1.17 × 10^5 M^{-1} cm^{-1}); λ_{max} (CD_2Cl_2): 568 nm (ε = 1.26 × 10^5 M^{-1} cm^{-1}); HRMS (ESI) m/z: 407.1022 (calcd for $C_{23}H_{23}N_2{}^{80}Se^+$, 407.1021).

SEHRS Substrate Preparation. Ag nanoparticle (NP) colloidal suspensions were synthesized via the Lee and Meisel method.[31] Specifically, 91.8 mg of silver nitrate was added to 200 mL of boiling water along with 115 mg of tribasic sodium citrate and allowed to boil for 30 min, then diluted to 1 L. 10^{-5} M aqueous solutions of TMR dyes were made with ultrapure water (18 MΩ cm), and mixed with Ag NP colloids to make 10^{-6} M dye adsorbed Ag NP solutions. The colloids were then destabilized with 1 M NaBr, resulting in Ag NP aggregations.

Experimental Spectroscopies. Absorption measurements were taken in 1 mm path length quartz cuvettes containing 5 × 10^{-5} M dye solutions in MeOH.

SERS spectra were acquired with a 532 nm diode-pumped solid-state laser (Spectra-Physics) and focused into an inverted microscope with 50 μW of power at the objective (Nikon Ti-U, 20×, NA = 0.5). The backscattered radiation is then passed through a Rayleigh rejection filter (Semrock) and dispersed with a spectrometer (Princeton Instruments Acton SP2300, f = 0.3 mm 1200 g/mm). The photons are then detected with a back illuminated, deep depletion CCD (PIXIS Spec-10 Princeton Instruments) and analyzed using Winspec32 software (Princeton Instruments).

The SEHRS spectra were taken using an optical parametric oscillator (APE picoEmerald), focused with an inverted microscope objective (Nikon Ti-U, 20×, NA = 0.5) with 2 mW of power at the objective. The backscattered radiation is collected and passed through a Rayleigh rejection filter (Semrock) and dispersed with a spectrometer (Princeton Instruments Acton SP2300, 1200 g/mm, BLZ = 500). The scattered photons are then detected with a back illuminated, deep depletion CCD (Excelon) and analyzed using Winspec32 software (Princeton Instruments). Spectra were recorded at laser wavelengths between 840−990 nm, 1064 nm, and 1150−1266 nm in 10 nm increments. Additional SEHRS and HR scans were taken with a Ti:sapphire picosecond tunable laser (Spectra-Physics Tsunami), pumped with a 532 nm laser (Spectra Physics Millennia Pro), at incident wavelengths from 1000 to 1030 nm in 10 nm increments. Solution-phase HR scans (i.e., no surface-enhancement) were taken using the Ti:sapphire set up with a typical power of 250 mW at the objective. The data were then analyzed and plotted in IgorPro (WaveMetrics).

COMPUTATIONAL METHODS

HR absolute intensities can be represented as their differential scattering cross sections

$$\frac{d\sigma^{HRS}}{d\Omega} = \frac{16\pi^2 h^3 \alpha^3 \upsilon_s{}^4 P_i}{Nc^2 e^6} \langle \beta'_{\alpha\beta\gamma} \rangle^2 \quad (4)$$

where h is Planck's constant, α is the fine structure constant, υ_s is the frequency of the scattered radiation, P_i is the initial vibrational state's population, N is the number of scatters per unit volume, 1 in this case, and c is the speed of light.[26,32,33] The transition hyperpolarizability term is defined as

$$\beta'_{\alpha\beta\gamma} = \sqrt{\frac{h}{8\pi^2 c \nu_a}} \frac{\partial \beta^{el}_{\alpha\beta\gamma}}{\partial Q_a} \quad (5)$$

where $\beta^{el}_{\alpha\beta\gamma}$ is the hyperpolarizability, Q_a is the normal mode of interest, and υ_a is the vibrational frequency of that mode.[34] This transition hyperpolarizability term is enclosed in brackets, indicating that the hyperpolarizability tensors are collected through averaging over all molecular orientations with respect to the incident light.[33] Hyperpolarizability derivatives were calculated using a damped quadratic response formalism and three-point finite-differentiation.[35] The use of damped response theory allowed for the equal treatment of resonance and non-RHR scattering based on a short-time approximation to RHR scattering.[36] In addition to the Franck−Condon (A) and Herzberg−Teller (B) scattering terms, all excited electronic states were accounted for in the simulations and average RHR spectra were produced. However, these simulations did not include other vibronic effects.[37]

A local version of the Dalton 2017 electronic structure program was used in conjunction with a local version of the Northwest Computational Chemistry Package (NWChem) 6.6 for all quantum mechanical calculations.[38,39] Geometry optimization calculations were done in NWChem utilizing the B3LYP exchange correlation (XC) potential and the 6-311G* basis set. For the geometry optimization, the numerical integration of the XC potential was done with an xfine grid, and the GMAX, GRMS, XMAX, and XRMS were all tightened to 0.000015, 0.00001, 0.0001, and 0.0001, respectively. In Dalton, transition hyperpolarizabilities were obtained by finite differentiation of the hyperpolarizabilities utilizing the same XC-potential and basis set mentioned previously. The one- and two-photon absorption calculations were also done in Dalton. No symmetry was assumed in all calculations. Surface selection rules are implicitly taken into account in accordance with a previous R6G surface geometry study.[40] Solvent effects are not taken into account, and calculated normal mode frequencies were scaled by a constant factor of 0.97.

DOI: 10.1021/acs.jpcc.8b07507
J. Phys. Chem. C 2018, 122, 25051−25058

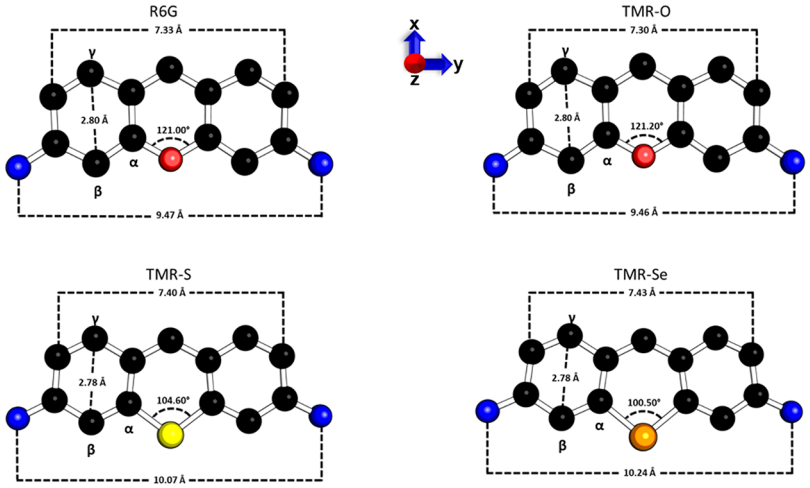

Figure 1. Theoretical structures of R6G and the TMR dyes. The phenyl group has been removed for clarity, leaving only the xanthene ring and nitrogen atoms of the appending amine groups. Several important structural parameters are labeled, such as the angle about the chalcogen atom and three distances that illustrate the distortion of the xanthene ring. The coordinate axis used throughout the manuscript appears in the top center. The greatest structural change is seen from **TMR-O** to **TMR-S**, while **TMR-S** and **TMR-Se** are very similar.

Table 1. Calculated and Experimental Absorption λ_{max} Values, Oscillator Strength, Transition Dipole Moment in the *y* Direction, Two-Photon Absorption Cross Section, and Two-Photon Absorption Tensor Values

	R6G	TMR-O	TMR-S	TMR-Se
experimental absorption (eV)	2.35	2.25	2.17	2.13
theoretical absorption (eV)	2.89	2.76	2.67	2.64
oscillator strength	0.74	0.77	0.70	0.71
transition dipole moment, *y* direction (au)	−3.24	3.37	3.28	3.30
TPA cross section (au)	7.79	8.68	2.50	1.71
TPA tensor: S_{yy}, S_{xy}	0.7, 67.2	0.4, −76.3	0.0, 42.4	1.1, −35.1

RESULTS AND DISCUSSION

Figure 1 displays the structural parameters of the dye molecules optimized at the B3LYP/6-311G* level of theory. The distance between the nitrogen atoms on the xanthene ring is about equal (∼9.46 Å) when comparing R6G to **TMR-O**; however, this distance increases to 10.07 and 10.24 Å for the S to Se analogue, respectively. Introduction of a larger heteroatom to the xanthene ring further expands the ring system and shortens the vertical distance between the β and γ carbons by about 0.02 Å. The angle about the chalcogen also contracts from ∼120° to about 104° and 100° when the O atom is exchanged for S and Se, respectively. From this analysis, it is clear that the most significant structural changes occur when O is replaced by S, and only minor changes occur between the S and Se analogues. Importantly, the structural modifications are symmetric about the center of the xanthene ring upon the addition of a larger chalcogen atom. Throughout this work, we will draw a connection between these structural parameters and the optical properties.

Table 1 summarizes properties related to the one- and two-photon absorption spectra of the TMR series. As the heteroatom (O) is substituted with an increasingly larger chalcogen, the energy of S_1 decreases in both the theoretical and experimental data. The ∼0.5 eV difference between the experiment and theory is likely due to solvent effects and approximations in the DFT methods. For one-photon absorption, the transition dipole moment is along the y direction (see Figure 1 for axes) and is largest for **TMR-O**, becoming smaller for the S and Se analogues as well as for R6G. For two-photon absorption, the cross section is largest for **TMR-O** and decreases significantly for the S and Se analogues, which corresponds with the decreasing oscillator strength. Experimental relative HR ratios and theoretical HR cross sections were measured to examine the trend of HR scattering efficiencies for the dye series. Experimentally, the ratio value is calculated by dividing the area of the most intense peak in the solution phase TMR HR spectrum by the area of the 1588 cm^{-1} peak in the crystal violet spectrum, which serves as a reference. Details of this procedure are given in the Supporting Information. The experimental ratios decrease from 1.35, to 0.70, and to 0.29 for the O, S, and Se analogues, respectively. The theoretical HR cross section also decreases from 1.88 for **TMR-O** to 1.11 for **TMR-S** and to 0.91 for **TMR-Se** in units of 10^{-59} cm^4 s/srad, indicating that the trend in the HR scattering efficiency is consistent in both theory and experiment.

The experimentally measured SERS and SEHRS of the TMR series, illustrated in Figure 2, are obtained on resonance with the lowest-lying electronic state (S_1), which is strongly one-photon allowed. The SERS and SEHRS spectra are recorded using the same excitation energy (i.e., 532 and 1064 nm respectively) to allow a direct comparison. If only one electronic state contributes to the resonance scattering process and *A*-term scattering is the dominant enhancement mechanism, then the SERS and SEHRS should display nearly equivalent relative intensities of the vibrational bands, as these are determined only by the Franck−Condon overlap.[22,41,42] The centrosymmetry of the xanthene ring constrains the one- and two-photon allowed states to be mutually exclusive, thus the S_1 state is the only contributor. The spectra in Figure 2

DOI: 10.1021/acs.jpcc.8b07507
J. Phys. Chem. C 2018, 122, 25051−25058

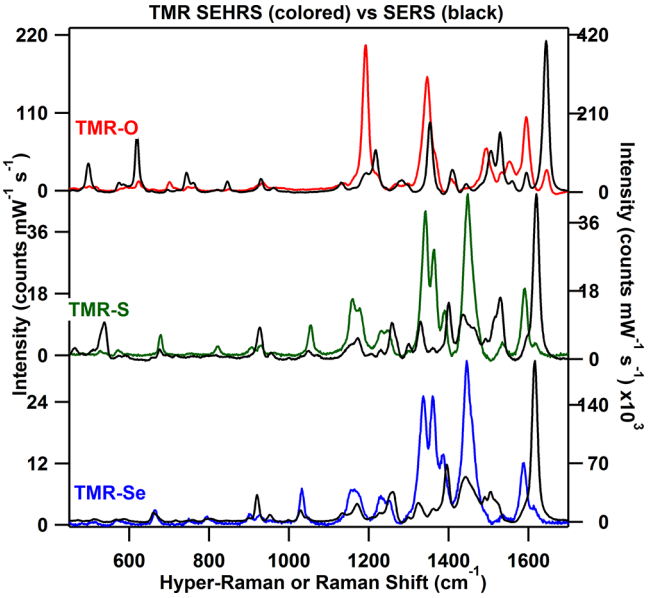

Figure 2. Experimental SEHRS (colored trace) and SERS (black trace) spectra taken at equal excitation energies of **TMR-O** (top), **TMR-S** (middle), and **TMR-Se** (bottom). Significant differences are observed between the SEHRS and SERS indicating *B*-term activity. The similarity of the **TMR-S** and **TMR-Se** spectra is attributed to their similar molecular geometry, see Figure 1.

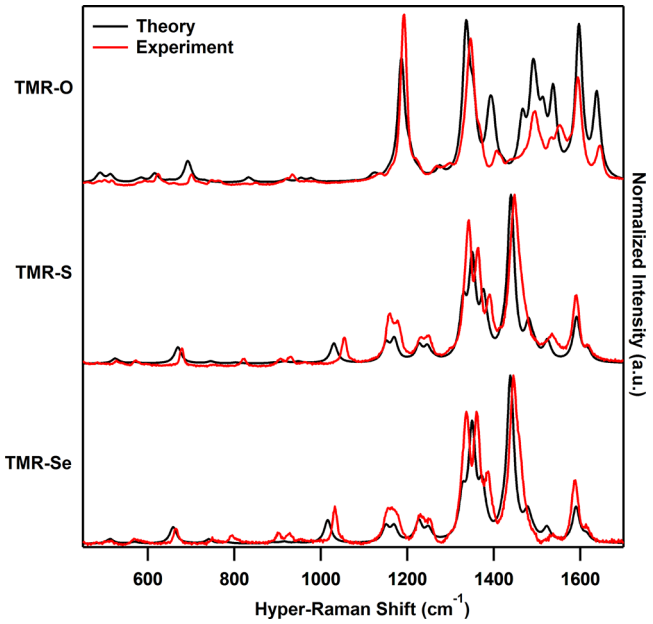

Figure 3. Comparison of experimental SEHRS spectra (red trace) obtained at 1064 nm and theoretical HR spectra (black trace) obtained from TDDFT calculations of **TMR-O** (top), **TMR-S** (center), and **TMR-Se** (bottom). Both experimental and theoretical spectra are normalized such that the highest intensity is set to 1.

exhibit obvious differences between the one- and two-photon scattering spectra, suggesting that strong *B*-term activity is present. Further consequences of this are observed in the changing SEHRS response as the larger heteroatom is introduced, which can be attributed to structural modifications of the xanthene ring. As discussed above (Figure 1), the introduction of the larger S heteroatom disturbs the nearly C_s symmetry of the xanthene ring. This plays an important role in the scattering mechanism because our calculations indicate that the electronic states of the TMRs are primarily located on the xanthene ring. This structural-based argument persists when Se is substituted for S, because the Se minimally disturbs the xanthene ring compared with the S analogue. Accordingly, the SEHRS spectra of **TMR-S** and **TMR-Se** on resonance with S_1 are extremely similar, having a correlation coefficient of 0.98. The theoretical calculations including the *B*-terms, shown in Figure 3, illustrate a close agreement between experimental and theoretical SEHRS spectra, further supporting the presence of non-Condon scattering in these molecules.

The theory additionally provides a description of the interplay between the vibrations of the TMRs and their electronic orbitals. Similar to previous work, difference HOMO orbitals were obtained by taking the difference between the absolute values of the perturbed HOMO orbitals using NWChem.[26] The perturbed orbitals were acquired by displacing the geometry of the molecule along the normal coordinates with a step size of ±10% of the normal mode displacements. Calculations show that the HR efficiency of these dyes can be attributed to the strong S_{xy} versus the weak S_{yy} components of the transition tensor. *A*-term scattering is weaker in this case because the one-photon transition moment is along the *y* direction, whereas the two-photon transition moment is dominated by the *xy* component. While these two transition moments alone will not couple together to give a large HR intensity, the molecular vibrations can couple the one- and two-photon transition moments. Similar to previous work on R6G, the TMRs' lowest unoccupied molecular orbitals (LUMOs) are symmetric about the center of the xanthene ring, while the HOMOs are antisymmetric.[26,43] This configuration leads to a two-photon weak but one-photon strong transition from HOMO to LUMO. The two-photon transition, however, can gain intensity through coupling with asymmetric vibrations which perturb the HOMO orbitals.

Analysis of the perturbed HOMO orbitals obtained through vibronic coupling provides additional RHR intensity. Figure 4

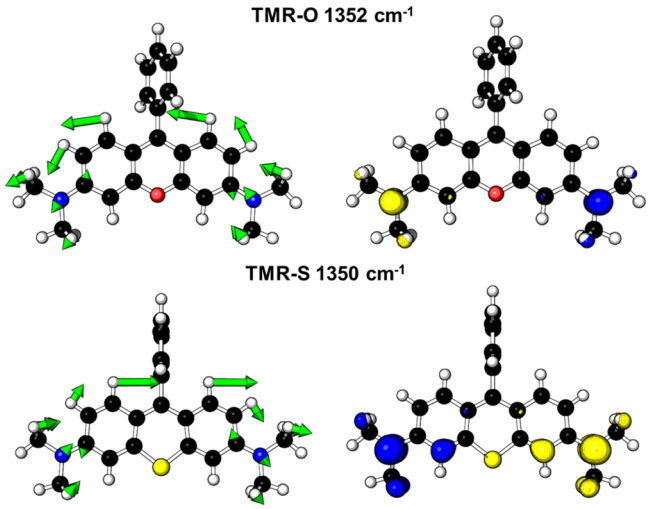

Figure 4. Vibrational mode vectors and difference HOMO images for mode 1352 cm^{-1} in **TMR-O** (top) and mode 1350 cm^{-1} for **TMR-S** (bottom). Blue represents a positive change in orbital asymmetry and yellow represents a negative change. The size of the difference orbitals is well correlated with the intensity of the associated vibrational band in the SEHRS spectra.

DOI: 10.1021/acs.jpcc.8b07507
J. Phys. Chem. C 2018, 122, 25051−25058

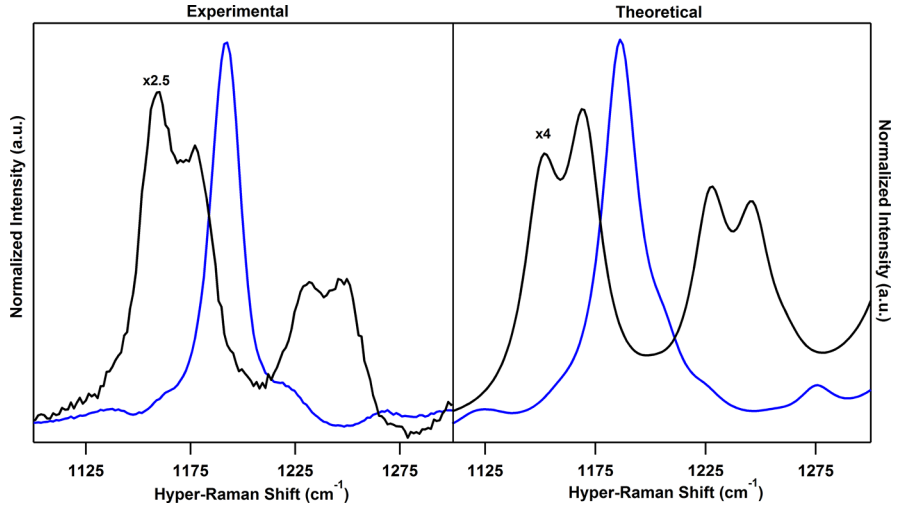

Figure 5. Experimental (left) and theoretical (right) normalized SEHRS spectra showing splitting of the 1186 cm^{-1} mode in **TMR-O** (blue) into two doublet modes for **TMR-S** (black). Both theory and experiment are normalized such that the highest intensity is set to 1. **TMR-S** spectra were multiplied by 2.5 for experimental and by 4 for the theoretical to highlight the correlation between difference orbital size and mode intensity and to clearly show the splitting that results from the distortion induced by the larger chalcogen.

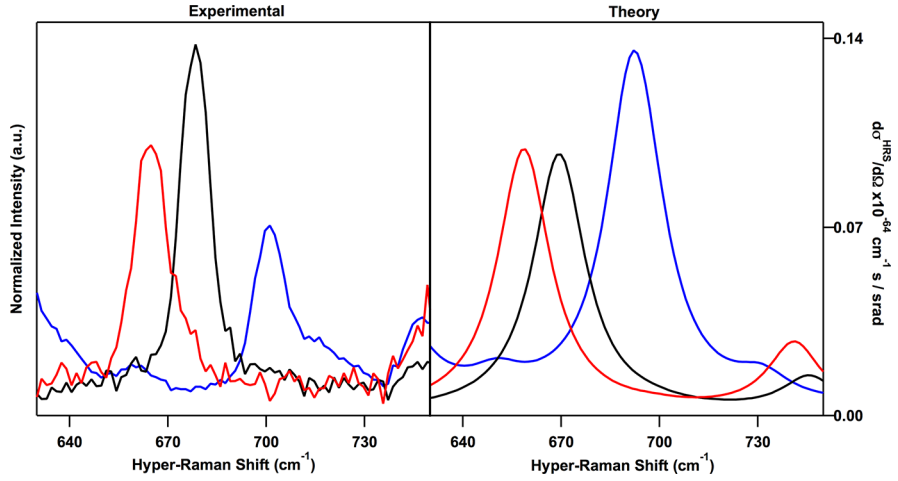

Figure 6. Experimental (left) and theoretical (right) SEHRS showing a progressive red shift of the 692 cm^{-1} mode in **TMR-O** (blue) to 669 cm^{-1} in **TMR-S** (black) and 659 cm^{-1} in **TMR-Se** (red).

illustrates the vibrational mode vectors and difference HOMO images for 1352 cm^{-1} mode of **TMR-O** and 1350 cm^{-1} of **TMR-S**. In this case, the difference orbitals are both anti-symmetric, but they are smaller in **TMR-O** (Figure 4, top). Using the calculated HOMO differences, the RHR intensity can be predicted by the symmetry and size of the HOMO difference orbitals. Comparing the 1350−1352 cm^{-1} modes, the difference ratio is 1.71, which corresponds to the predicted RHR intensity ratio and is close to the experimentally observed ratio, 2.06. Through these calculations of vibrational modes and associated difference HOMO images, a complete picture of the vibrations and their effects on the excited-state landscape can be accurately predicted.

To further explain the heteroatom's effect on the vibronic enhancement mechanism, two further examples of mode analysis are presented. Case one follows the 1186 cm^{-1} vibrational mode of **TMR-O** (Figure 5). As S is substituted in place of O, the ring perturbations induce a splitting of the 1186 cm^{-1} mode in **TMR-O** into two doublets, one red-shifted and one blue-shifted. These four modes have difference orbitals that are smaller than those of 1186 cm^{-1}, which coincides with their weaker peak intensity. This splitting is further observed for the Se analogue, an expected result following our structural explanation. The HOMO difference orbitals and vibrational vector images for the 1186 cm^{-1} mode and the four modes it split into for **TMR-Se** are in the Supporting Information.

The second case follows the lower energy modes appearing in the 640−700 cm^{-1} range, where there are three modes that can be tracked across all three dyes' RHR spectra (Figure 6). The short wavelength mode 692 cm^{-1} for **TMR-O** is present for all analogues, however, a blue shift occurs to S (669 cm^{-1}) and Se (659 cm^{-1}). In this case the vibrations are very similar, but the magnitude of the orbital difference increases slightly with the larger heteroatom. The vibrational mode vectors and HOMO difference images can be found in the Supporting Information.

■ CONCLUSIONS

In this work, we explore how systematic structural changes to rhodamine-derivatives affect the nonlinear scattering of

DOI: 10.1021/acs.jpcc.8b07507
J. Phys. Chem. C 2018, 122, 25051−25058

vibrational states. For the TMR series, the introduction of a larger chalcogen to the xanthene ring induces structural changes significant enough to perturb the orbital symmetry. These perturbations result in several ring vibrational modes splitting into additional modes as well as a shift in energy. We have further shown that the symmetry and size of the HOMO difference orbitals can be used to predict the strength of the RHR scattering response. This combined analysis utilizes experimental and theoretical techniques to analyze vibrational normal modes and the vibrationally induced changes to the highest occupied molecular orbitals. We believe that the correlation between structural geometry and nonlinear properties explored here for a series of rhodamine derivatives provides insights into future efforts to design two-photon bright compounds.

■ ASSOCIATED CONTENT

Supporting Information

The Supporting Information is available free of charge on the ACS Publications website at DOI: 10.1021/acs.jpcc.8b07507.

Additional details on the experimental determination of the HR cross section ratios as well as the full wavelength dependence of the SEHRS spectra (840−1266 nm). On- and off-resonance SEHRS spectra of the TMR dyes are included in figure S1. Vibrational mode vector diagrams and orbital difference plots of the vibrational modes mentioned in Figures 5 and 6 are included as Figures S2 and S3. Mass spectra and NMR data are included for all TMRs (PDF)

■ AUTHOR INFORMATION

Corresponding Authors

*E-mail: mdetty@buffalo.edu (M.R.D).
*E-mail: jensen@chem.psu.edu (L.J.).
*E-mail: jon.camden@nd.edu (J.P.C.).

ORCID

Jacob E. Olson: 0000-0001-7110-1739
Michael R. Detty: 0000-0002-8815-1481
Lasse Jensen: 0000-0003-1237-5021
Jon P. Camden: 0000-0002-6179-2692

Author Contributions

The manuscript was written through contributions of all authors. All authors have given approval to the final version of the manuscript.

Notes

The authors declare no competing financial interest.

■ ACKNOWLEDGMENTS

This material is based upon work supported by the National Science Foundation under grant numbers CHE-1709566 (J.E.O., J.P.C.), CHE-1362825 (A.T., Z.H., L.J.), and CHE 1566142 (M.K.L. and M.R.D.). Any opinions, findings, and conclusions or recommendations expressed in this material are those of the authors and do not necessarily reflect the views of the National Science Foundation. This work was also supported by the University of Notre Dame (J.P.C. and J.E.O.), and portions of this work were conducted with Advanced CyberInfrastructure computational resources provided by The Institute for CyberScience at The Pennsylvania State University (http://ics.psu.edu).

■ REFERENCES

(1) Dai, C.-G.; Wang, J.-L.; Fu, Y.-L.; Zhou, H.-P.; Song, Q.-H. Selective and Real-Time Detection of Nitric Oxide by a Two-Photon Fluorescent Probe in Live Cells and Tissue Slices. *Anal. Chem.* **2017**, *89*, 10511−10519.

(2) Liu, Q.; Guo, B.; Rao, Z.; Zhang, B.; Gong, J. R. Strong Two-Photon-Induced Fluorescence from Photostable, Biocompatible Nitrogen-Doped Graphene Quantum Dots for Cellular and Deep-Tissue Imaging. *Nano Lett.* **2013**, *13*, 2436−2441.

(3) Sarkar, A. R.; Heo, C. H.; Lee, H. W.; Park, K. H.; Suh, Y. H.; Kim, H. M. Red Emissive Two-Photon Probe for Real-Time Imaging of Mitochondria Trafficking. *Anal. Chem.* **2014**, *86*, 5638−5641.

(4) Zhou, L.; Wang, Q.; Zhang, X.-B.; Tan, W. Through-Bond Energy Transfer-Based Ratiometric Two-Photon Probe for Fluorescent Imaging of Pd2+ Ions in Living Cells and Tissues. *Anal. Chem.* **2015**, *87*, 4503−4507.

(5) Heiner, Z.; Gühlke, M.; Živanović, V.; Madzharova, F.; Kneipp, J. Surface-Enhanced Hyper Raman Hyperspectral Imaging and Probing in Animal Cells. *Nanoscale* **2017**, *9*, 8024−8032.

(6) He, G. S.; Zhu, J.; Baev, A.; Samoć, M.; Frattarelli, D. L.; Watanabe, N.; Facchetti, A.; Ågren, H.; Marks, T. J.; Prasad, P. N. Twisted π-System Chromophores for All-Optical Switching. *J. Am. Chem. Soc.* **2011**, *133*, 6675−6680.

(7) Castet, F.; Rodriguez, V.; Pozzo, J.-L.; Ducasse, L.; Plaquet, A.; Champagne, B. Design and Characterization of Molecular Nonlinear Optical Switches. *Acc. Chem. Res.* **2013**, *46*, 2656−2665.

(8) Shiring, S. B.; Gieseking, R. L.; Risko, C.; Brédas, J.-L. Assessment of Front-Substituted Zwitterionic Cyanine Polymethines for All-Optical Switching Applications. *J. Phys. Chem. C* **2017**, *121*, 14166−14175.

(9) Shalav, A.; Richards, B. S.; Green, M. A. Luminescent Layers for Enhanced Silicon Solar Cell Performance: Up-Conversion. *Sol. Energy Mater. Sol. Cells* **2007**, *91*, 829−842.

(10) van der Ende, B. M.; Aarts, L.; Meijerink, A. Lanthanide Ions as Spectral Converters for Solar Cells. *Phys. Chem. Chem. Phys.* **2009**, *11*, 11081−11095.

(11) Huang, X.; Han, S.; Huang, W.; Liu, X. Enhancing Solar Cell Efficiency: The Search for Luminescent Materials as Spectral Converters. *Chem. Soc. Rev.* **2013**, *42*, 173−201.

(12) He, G. S.; Tan, L.-S.; Zheng, Q.; Prasad, P. N. Multiphoton Absorbing Materials: Molecular Designs, Characterizations, and Applications. *Chem. Rev.* **2008**, *108*, 1245−1330.

(13) Kelley, A. M. Hyper-Raman Scattering by Molecular Vibrations. *Annu. Rev. Phys. Chem.* **2010**, *61*, 41−61.

(14) Cyvin, S. J.; Rauch, J. E.; Decius, J. C. Theory of Hyper-Raman Effects (Nonlinear Inelastic Light Scattering): Selection Rules and Depolarization Ratios for the Second-Order Polarizability. *J. Chem. Phys.* **1965**, *43*, 4083−4095.

(15) Golab, J. T.; Sprague, J. R.; Carron, K. T.; Schatz, G. C.; Van Duyne, R. P. A surface enhanced hyper-Raman scattering study of pyridine adsorbed onto silver: Experiment and theory. *J. Chem. Phys.* **1988**, *88*, 7942−7951.

(16) Yang, W.-H.; Schatz, G. C. Ab initio and semiempirical molecular orbital studies of surface enhanced and bulk hyper-Raman scattering from pyridine. *J. Chem. Phys.* **1992**, *97*, 3831−3845.

(17) Milojevich, C. B.; Mandrell, B. K.; Turley, H. K.; Iberi, V.; Best, M. D.; Camden, J. P. Surface-Enhanced Hyper-Raman Scattering from Single Molecules. *J. Phys. Chem. Lett.* **2013**, *4*, 3420−3423.

(18) Trujillo, M. J.; Camden, J. P. Utilizing Molecular Hyperpolarizability for Trace Analysis: A Surface-Enhanced Hyper-Raman Scattering Study of Uranyl Ion. *ACS Omega* **2018**, *3*, 6660−6664.

(19) [In This Work, We Exclusive Consider Systems on Resonance, I.E. Surface-Enhanced Resonance Hyper-Raman Scattering, but We Still Refer to These as Sehrs Spectra.].

(20) Chung, Y. C.; Ziegler, L. D. The vibronic theory of resonance hyper-Raman scattering. *J. Chem. Phys.* **1988**, *88*, 7287−7294.

(21) Silverstein, D. W.; Jensen, L. Vibronic Coupling Simulations for Linear and Nonlinear Optical Processes: Theory. *J. Chem. Phys.* **2012**, *136*, 064111.

DOI: 10.1021/acs.jpcc.8b07507
J. Phys. Chem. C 2018, 122, 25051−25058

(22) Baranov, A.; Bobovich, Y. S. Super-Enhanced Hyper-Raman Scattering from Dyes Adsorbed on Colloidal Silver Particles. *J. Exp. Theor. Phys.* **1982**, *36*, 339−343.
(23) Wakebe, T.; Van Keuren, E. The Excitation Spectra of Two-Photon Induced Fluorescence in Xanthene Dyes. *Jpn. J. Appl. Phys.* **1999**, *38*, 3556−3561.
(24) Wolff, J. J.; Wortmann, R. Organic Materials for Second-Order Non-Linear Optics. *Adv. Phys. Org. Chem.* **1999**, *32*, 121−217.
(25) Milojevich, C. B.; Silverstein, D. W.; Jensen, L.; Camden, J. P. Probing Two-Photon Properties of Molecules: Large Non-Condon Effects Dominate the Resonance Hyper-Raman Scattering of Rhodamine 6g. *J. Am. Chem. Soc.* **2011**, *133*, 14590−14592.
(26) Milojevich, C. B.; Silverstein, D. W.; Jensen, L.; Camden, J. P. Surface-Enhanced Hyper-Raman Scattering Elucidates the Two-Photon Absorption Spectrum of Rhodamine 6g. *J. Phys. Chem. C* **2013**, *117*, 3046−3054.
(27) Ohulchanskyy, T. Y.; Donnelly, D. J.; Detty, M. R.; Prasad, P. N. Heteroatom Substitution Induced Changes in Excited-State Photophysics and Singlet Oxygen Generation in Chalcogenoxanthylium Dyes: Effect of Sulfur and Selenium Substitutions. *J. Phys. Chem. B* **2004**, *108*, 8668−8672.
(28) Detty, M. R.; Prasad, P. N.; Donnelly, D. J.; Ohulchanskyy, T.; Gibson, S. L.; Hilf, R. Synthesis, Properties, and Photodynamic Properties in Vitro of Heavy-Chalcogen Analogues of Tetramethylrosamine. *Bioorg. Med. Chem.* **2004**, *12*, 2537−2544.
(29) Ehrlich, P.; Benda, L. Über die Einwirkung von Cyankalium auf Pyronin- und Acridinium-Farbstoffe. *Chem. Ber.* **1913**, *46*, 1931−1951.
(30) Brennan, N. K.; Donnelly, D. J.; Detty, M. R. Selenoxanthones Via Directed Metalations in 2-Arylselenobenzamide Derivatives. *J. Org. Chem.* **2003**, *68*, 3344−3347.
(31) Lee, P. C.; Meisel, D. Adsorption and Surface-Enhanced Raman of Dyes on Silver and Gold Sols. *J. Phys. Chem.* **1982**, *86*, 3391−3395.
(32) Silverstein, D. W.; Jensen, L. Vibronic Coupling Simulations for Linear and Nonlinear Optical Processes: Simulation Results. *J. Chem. Phys.* **2012**, *136*, 064110.
(33) Ziegler, L. D. Hyper-Raman Spectroscopy. *J. Raman Spectrosc.* **1990**, *21*, 769−779.
(34) Quinet, O.; Champagne, B.; Van Gisbergen, S. J. A. Time-dependent density functional theory simulation of hyper-Raman spectra. *Int. J. Quantum Chem.* **2006**, *106*, 599−608.
(35) Hu, Z.; Autschbach, J.; Jensen, L. Simulation of Resonance Hyper-Rayleigh Scattering of Molecules and Metal Clusters Using a Time-Dependent Density Functional Theory Approach. *J. Chem. Phys.* **2014**, *141*, 124305.
(36) Jensen, L.; Zhao, L. L.; Autschbach, J.; Schatz, G. C. Theory and Method for Calculating Resonance Raman Scattering from Resonance Polarizability Derivatives. *J. Chem. Phys.* **2005**, *123*, 174110.
(37) Turley, H. K.; Hu, Z.; Silverstein, D. W.; Cooper, D. A.; Jensen, L.; Camden, J. P. Probing Two-Photon Molecular Properties with Surface-Enhanced Hyper-Raman Scattering: A Combined Experimental and Theoretical Study of Crystal Violet. *J. Phys. Chem. C* **2016**, *120*, 20936−20942.
(38) Valiev, M.; Bylaska, E. J.; Govind, N.; Kowalski, K.; Straatsma, T. P.; Van Dam, H. J. J.; Wang, D.; Nieplocha, J.; Apra, E.; Windus, T. L.; de Jong, W. A. Nwchem: A Comprehensive and Scalable Open-Source Solution for Large Scale Molecular Simulations. *Comput. Phys. Commun.* **2010**, *181*, 1477−1489.
(39) Aidas, K.; Angeli, C.; Bak, K. L.; Bakken, V.; Bast, R.; Boman, L.; Christiansen, O.; Cimiraglia, R.; Coriani, S.; Dahle, P.; et al. The Dalton Quantum Chemistry Program System. *Wiley Interdiscip. Rev.: Comput. Mol. Sci.* **2014**, *4*, 269−284.
(40) Turley, H. K.; Hu, Z.; Jensen, L.; Camden, J. P. Surface-Enhanced Resonance Hyper-Raman Scattering Elucidates the Molecular Orientation of Rhodamine 6g on Silver Colloids. *J. Phys. Chem. Lett.* **2017**, *8*, 1819−1823.
(41) Baranov, A. V.; Bobovich, Y. S.; Petrov, V. I. Spectroscopy of Resonance Hyper-Raman Scattering of Light. *Phys.-Usp.* **1990**, *33*, 812−832.
(42) Yu, N.-T.; Nie, S.; Lipscomb, L. A. Surface-enhanced hyper-Raman spectroscopy with a picosecond laser. New vibrational information for non-centrosymmetric carbocyanine molecules adsorbed on colloidal silver. *J. Raman Spectrosc.* **1990**, *21*, 797−802.
(43) Milojevich, C. B.; Silverstein, D. W.; Jensen, L.; Camden, J. P. Probing One-Photon Inaccessible Electronic States with High Sensitivity: Wavelength Scanned Surface Enhanced Hyper-Raman Scattering. *ChemPhysChem* **2011**, *12*, 101−103.

DOI: 10.1021/acs.jpcc.8b07507
J. Phys. Chem. C 2018, 122, 25051−25058